Origins of Heat Transport Anisotropy in $MoTe_2$ and Other Bulk Van der Waals Materials

Hongkun Li[1,4,5], Tribhuwan Pandey[2,6], Yi Jiang[1], Xiaokun Gu[3], Lucas Lindsay[2] and Yee Kan Koh[1,4*]

[1] Department of Mechanical Engineering, National University of Singapore, Singapore 117576

[2] Materials Science and Technology Division, Oak Ridge National Laboratory, Oak Ridge, Tennessee 37831, USA

[3] Institute of Engineering Thermophysics, School of Mechanical Engineering, Shanghai Jiao Tong University, Shanghai 200240, China

[4] Centre of Advanced 2D Materials, National University of Singapore, Singapore 117542

[5] School of Mechanical Engineering, Southwest Jiaotong University, Chengdu 610031, China

[6] Department of Physics, University of Antwerp, Groenenborgerlaan 171, B-2020 Antwerp, Belgium

*Corresponding Author: Yee Kan Koh, Email: mpekyk@nus.edu.sg

Abstract

Knowledge of how heat flows anisotropically in van der Waals (vdW) materials is crucial for thermal management of emerging 2D materials devices and design of novel anisotropic thermoelectric materials. Despite the importance, anisotropic heat transport in vdW materials is yet to be systematically studied and is often presumably attributed to anisotropic speeds of sound in vdW materials due to soft interlayer bonding relative to covalent in-plane networks of atoms. In this work, we investigate the origins of the anisotropic heat transport in vdW materials, through time-domain thermoreflectance (TDTR) measurements and first-principles calculations of anisotropic thermal conductivity of three different phases of $MoTe_2$. $MoTe_2$ is ideal for the study due to its weak anisotropy in the speeds of sound. We find that even when the speeds of sound are roughly isotropic, the measured thermal conductivity of $MoTe_2$ along the c-axis is 5-8 times lower than that along the in-plane axes. We derive meaningful characteristic heat capacity, phonon group velocity, and relaxation times from our first principles calculations for selected vdW materials ($MoTe_2$, BP, *h*-BN, and MoS_2), to assess the contributions of these factors to the anisotropic heat transport. Interestingly, we find that the main contributor to the heat transport anisotropy in vdW materials is anisotropy in heat capacity of the dominant heat-carrying phonon modes in different directions, which originates from anisotropic optical phonon dispersion and disparity in the frequency of heat-carrying phonons in different directions. The discrepancy in frequency of the heat-carrying phonons also leads to ~2 times larger average relaxation times in the cross-plane direction, and partially explains the apparent dependence of the anisotropic heat transport on the anisotropic speeds of sound. This work provides insight into understanding of the anisotropic heat transport in vdW materials.

Main Text

Van der Waals (vdW) materials (e.g., graphite, transition metal dichalcogenides, black phosphorus) consist of covalently bonded two-dimensional atomic layers (i.e., basal planes) that are weakly bound by van der Waals forces, forming layered crystal structures in the hexagonal, orthorhombic, monoclinic and triclinic crystal families. One consequence of the layered crystal structures is that the optical [1,2], electronic [3], thermal [4,5] and thermoelectric [6,7] properties of vdW materials can be highly anisotropic. For example, the in-plane thermal conductivities (Λ_a and Λ_b) along the crystallographic directions *a* and *b* in the basal planes are usually much higher than the cross-plane thermal conductivity (Λ_c) along the crystallographic direction *c* across the basal planes. The thermal conductivity anisotropy ratios of these vdW materials can be as high as ≈ 300 (e.g., $\Lambda_a/\Lambda_c \approx 300$ in graphite) while in-plane anisotropy only reaches <3 (e.g., $\Lambda_a/\Lambda_b \approx 3$ in black phosphorus). In this regard, the anisotropic thermal properties have been explored for novel applications of vdW materials, e.g., as directional heat spreaders [8] for thermal management of electronic devices and for more efficient thermoelectric energy conversion along particular directions [6,9]. Thus, it is crucial to understand the origins of the anisotropic heat transport.

Fundamentally, anisotropic heat transport in vdW materials is due to collective effects of *all* phonon modes (of different frequencies and directions). To illustrate this point, consider the thermal conductivity in any principal direction *i*, Λ_i (or in the tensor form $\Lambda_i = \Lambda_{i,i}$), given by [10],

$$\Lambda_i = \sum_q C_q \, v_q^2 \cos^2\theta_{q,i} \tau_q \quad (1)$$

where C_q, v_q, and τ_q are modal heat capacity, group velocity, and relaxation time of each phonon

mode q in the first Brillouin zone with different wavevectors and polarizations, and $\theta_{q,i}$ is the angle between the propagation direction of phonon mode q and the direction of applied temperature flux *i*. Here, we explicitly express $\left(\mathbf{v}_q \cdot \boldsymbol{i}\right)^2$ as $v_q^2 \cos^2\theta_{q,i}$ to isolate the effects of propagation direction from the amplitude of phonon velocity. We consider τ_q as determined in the relaxation time approximation [11] and thus it does not have explicit directional dependence. Transport lifetimes determined by full solution of the Boltzmann transport equation can vary depending on the direction of the applied temperature gradient. This ultimately leads to the same Eq. (1) except with lifetime calculated along direction *i*. As suggested by Eq. (1) heat is carried in direction *i* not only by phonons strictly propagating in direction *i* but also in large part by phonons propagating in all directions in a convoluted manner. Hence, there is no easy way to simplify Eq. (1) such that the different directional thermal conductivities depend only on the bulk material properties along their respective directions (e.g., speeds of sounds in high-symmetry crystallographic directions), and as a result, it is hard to isolate the contributions of individual properties to heat transport anisotropy.

Many prior studies [12-18], however, have made attempts to understand anisotropic heat transport in vdW materials in this way. For example, anisotropy in *in-plane* thermal conductivity (i.e., Λ_a/Λ_b) is often attributed to anisotropy in speeds of sound in the *in-plane* direction (e.g., $\bar{c}_a^2/\bar{c}_b^2$), due to good agreement between Λ_a/Λ_b and $\bar{c}_a^2/\bar{c}_b^2$ along the high-symmetry *a* and *b* directions according to the kinetic theory of phonons [12-14]. (Note that the average speed of sound $\bar{c}_i$ is gives a relatively simplistic measure of the effects of the more rigorous mode phonon velocities v_q in Eq. (1). It is often defined, here and elsewhere [13,18], as $\bar{c}_i^2=\frac{1}{3}\sum c_{i,\alpha}^2$, where $c_{i,\alpha}$ is the speed of sound of acoustic branch α (typically two transverse

and one longitudinal acoustic branch) along the high-symmetry crystallographic direction *i*, typically sampled near the Brillouin zone center.) However, as indicated in Eq. (1), the thermal conductivity in a high-symmetry direction should not only depend on the low-frequency phonons propagating along the direction, but on all phonons with some component of its velocity in this direction. Hence, the good agreement between $\bar{c}_a^2/\bar{c}_b^2$ and Λ_a/Λ_b may be coincidence, and other properties (e.g., phonon heat capacity and relaxation time) may also contribute to the anisotropy of heat transport. In fact, calculations using the Peierls-Boltzmann transport equation [5,19] and estimations from an anisotropic Callaway model [20] suggest that phonon relaxation times for phonons with wavevectors primarily in the *ab* plane can be substantially higher than those with wavevectors primarily along the *c* axis, and thus contribute to thermal conductivity anisotropy [19,21].

In this paper, we identify the main contributing material properties to the anisotropic heat transport, through time-domain thermoreflectance (TDTR) measurements and first-principles calculations of the anisotropic heat transport in three vdW layered phases of $MoTe_2$. We choose $MoTe_2$ for our studies because it has three stable phases with different crystal structures but similar speeds of sound along high-symmetry directions, and thus is a good platform to investigate the roles of phonon relaxation time and heat capacity to the anisotropic phonon transport in vdW materials. We find that contradictory to common beliefs, the thermal conductivity anisotropy in vdW materials is primarily originated from anisotropy in the mode heat capacity of phonons contributing to heat transport in respective directions. In this context, we further discuss how phonon velocities and relaxation times contribute to the thermal conductivity anisotropy. Our work provides valuable insights into the origins of anisotropic heat

transport.

We examine all three phrases of $MoTe_2$, i.e., hexagonal $MoTe_2$ of the $P6_3/mmc$ group (2H-$MoTe_2$), orthorhombic $MoTe_2$ of the $Pmn2_1$ group (Td-$MoTe_2$) and monoclinic $MoTe_2$ of the $P2_1/m$ group (1T′-$MoTe_2$). Section S1 of Supplementary Material (SM) give descriptions of the crystal structures these phases. We note that 2H-$MoTe_2$ and 1T′-$MoTe_2$ are thermodynamically stable at 300 K, while a phase transition from the 1T′ phase to the Td phase occurs at ≈ 250 K [22]. In this work, heat transport anisotropies are discussed for 2H phase and 1T′ phase at 300 K, and for Td phase at 80 K. Due to crystal symmetry, only the 1T′ and Td phases exhibit anisotropy in the thermal conductivity in the basal plane. We carefully verify the existence of the $MoTe_2$ phases in our samples at 300 K and 80 K, and determine orientations for our measurements by Raman spectroscopy, see Figures S1(c) and (d) in Section S1 of SM.

We measured the in-plane thermal conductivity (Λ_a, Λ_b) and cross-plane thermal conductivity (Λ_c) of all three phases of $MoTe_2$ by beam-offset TDTR and TDTR, respectively. Details of TDTR and beam-offset TDTR can be found in Methods and Section S2 in SM. We performed TDTR and beam-offset TDTR measurements using a wide range of modulation frequencies (0.2 MHz < f < 10 MHz) and $1/e^2$ laser beam radii (2.5 μm < w_0 < 25 μm) to ensure that the reported thermal conductivity is not affected by experimental artifacts due to non-equilibrium phonons [23-26], see Section S3 in SM for discussion on frequency and spot size dependence of our measurements. The uncertainty of our measurements is around 15 %. We also note that accurate Λ_c of $MoTe_2$ can only be derived from TDTR measurements performed using a sufficiently low f. For example, prior measurements of Λ_c of 2H-$MoTe_2$ by Yan *et al*. [27] using a high modulation frequency of f ≈ 10 MHz, similar to our measurements at the same

f, is ≈ 40% lower than the intrinsic values reported in this work.

We show our in-plane thermal conductivity (Λ_a, Λ_b) and cross-plane thermal conductivity (Λ_c) measurements of 2H-$MoTe_2$ and 1T′-$MoTe_2$ as a function of temperature in Figures 1(a) and 1(b), respectively. For comparison, we also include prior first-principles calculations of $MoTe_2$ [28] and prior measurements of other bulk vdW materials (i.e., graphite [29], BP [5], MoS_2 [4], $MoSe_2$ [4], WS_2 [4], WSe_2 [4,30], and WTe_2 [31]), also plotted as a function of temperature. For 2H-$MoTe_2$, our measured Λ_c and Λ_a agree reasonably well with the first principles calculations by Lindroth *et al.* [28], see Figure 1. We find that both Λ_c and Λ_a of 2H-$MoTe_2$ exhibit a T^{-1} temperature dependence, which suggests that phonon scatterings are dominated by Umklapp processes along both crystallographic orientations. For 1T′-$MoTe_2$ and Td-$MoTe_2$, measured Λ is substantially smaller than that of 2H-$MoTe_2$, likely due to stronger scattering of acoustic phonons by optical phonons in their more complex crystal structures [32,33]. The strong scattering of acoustic phonons is further demonstrated in the weak, glass-like temperature dependence of Λ_a, Λ_b, and Λ_c of 1T′-$MoTe_2$ and Td-$MoTe_2$, which is consistent with the prior measurements by Yan *et al.* [27], see Figure 1. Similar weak temperature dependence of Λ was found in other complex, low-symmetry (monoclinic or orthorhombic) crystals, e.g., $NaNbO_3$ [34], $CsBiNb_2O_7$ [35] and clathrates [36,37]. Interestingly, we do not observe any abrupt changes of Λ in the temperature range of the phase transition of 1T′-$MoTe_2$ at 250 K. The continuous Λ suggests that the slightly different crystal structures of 1T′- and Td-$MoTe_2$ do not significantly affect phonon scattering in the materials.

We show the cross-plane (black) and in-plane (red) anisotropy in the measured Λ of 2H, 1T′, and Td-$MoTe_2$ in Figure 1(c). We find that while the in-plane anisotropy in Λ does not

depend on temperature, temperature dependence is observed for the cross-plane anisotropy. Since the phonon dispersion is not expected to change significantly with temperature, little temperature dependence of the anisotropic heat transport should be observed if this is governed by anisotropy in the speeds of sound alone. Thus, the observed temperature dependence of the anisotropy further suggests that, in additional to speeds of sound, other factors may be contributing to thermal transport anisotropy.

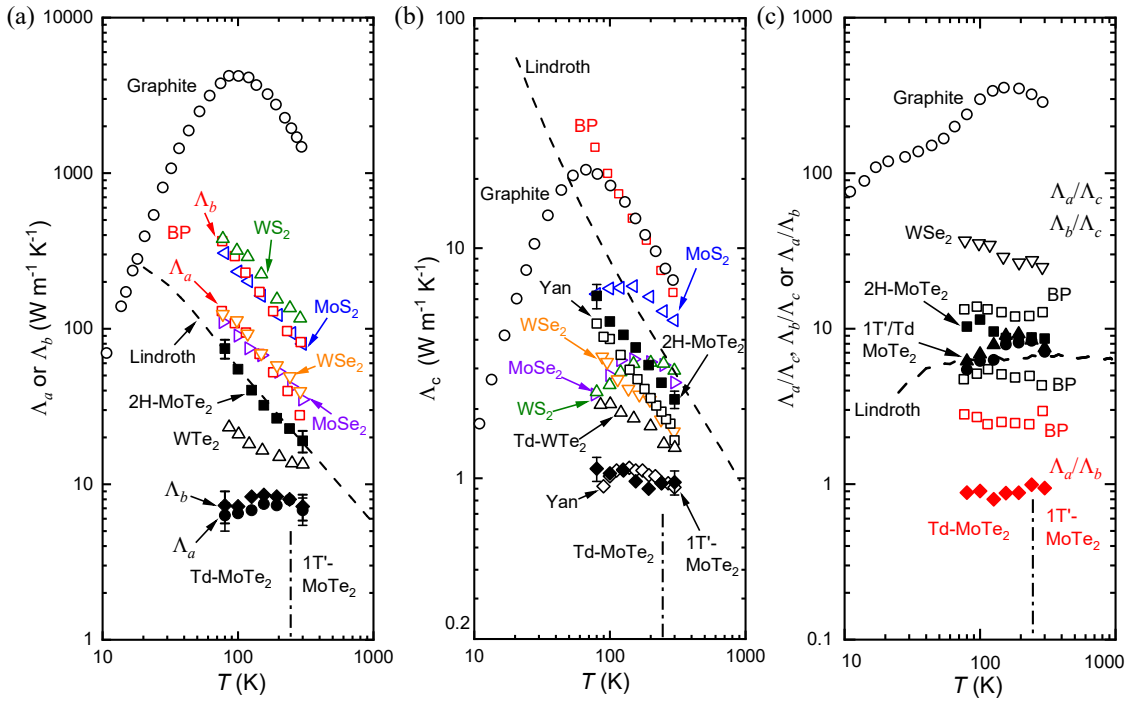

Figure 1. (a) Temperature dependence of in-plane thermal conductivity Λ_a and Λ_b measurements of 2H-, 1T′-, and Td-$MoTe_2$ (solid black symbols, this work), compared to prior measurements of graphite (open circles, [29]), BP (red squares, [5]), WTe_2 (open black triangles, [31]) and other vdW materials (as labelled, [4]). Solid circles and solid diamonds represent Λ_a and Λ_b, respectively. **(b)** Temperature dependence of cross-plane thermal conductivity Λ_c measurements of 2H-, 1T′- and Td-$MoTe_2$ (solid black symbols, this work), compared to the previous measurements of 2H-$MoTe_2$ (open squares, [27]), 1T′ and Td-$MoTe_2$ (open diamonds, [27]), graphite (open circles, [29]), BP (red squares, [5]), WSe_2 (orange down triangles, [30])

and other vdW materials (as labelled, [4]). **(c)** Temperature dependence of anisotropy of selected vdW materials, derived from measurements in (a) and (b). Red symbols are in-plane anisotropy, while black symbols are cross-plane anisotropy. In all figures, the dashed lines are first principles calculations of 2H-$MoTe_2$ by Lindroth *et al.* [28], and the dot-dash vertical lines indicate the phase transition temperature at ≈ 250 K.

To assess whether the anisotropy in the thermal conductivity is mainly due to anisotropy in speeds of sound as previously suggested [12-16], we compare the in-plane (Λ_a/Λ_b) and cross-plane (Λ_a/Λ_c) anisotropy in our thermal conductivity measurements of 2H- and 1T′-$MoTe_2$ at 300 K and Td-$MoTe_2$ at 80 K, to the anisotropy in speeds of sound in Table 1. We derived the average speeds of sound from our first principles calculations (see Methods and Table S1 in Section S4 of SM for our calculated values of speeds of sound for all phases of $MoTe_2$) using $\bar{c}_i^2=\frac{1}{3}\sum c_{i,\alpha}^2$ (We note that other expressions of average speeds of sound have been in the literature, see Refs. [15-17,38]. Here, we choose this expression as it is the most commonly used. Choosing other expressions for $\bar{c}_i$ does not affect the conclusions drawn here, see Table S2 in Section S4 of SM). We find that in the basal planes, Λ_a/Λ_b approximates to $\bar{c}_a^2/\bar{c}_b^2$ for both 1T′-$MoTe_2$ and Td-$MoTe_2$ phases. However, across the basal planes, $\bar{c}_a^2/\bar{c}_c^2$ and $\bar{c}_b^2/\bar{c}_c^2$ are < 2.2, while the anisotropy of the thermal conductivity (i.e., Λ_a/Λ_c and Λ_b/Λ_c) can range up to ≈ 8, see Table 1.

The distinctive behavior between anisotropy in and across the basal planes is not unique to $MoTe_2$. To illustrate the stark difference between the in-plane and cross-plane anisotropy, we compile the cross-plane (black symbols) and in-plane (red symbols) thermal conductivity anisotropies for a wide range of vdW materials as a function of $\bar{c}_i^2/\bar{c}_j^2$, in Figure

2. We derive the average speeds of sound of the materials from our calculations and prior first principles calculations of phonon dispersions and experimental measurements of elastic stiffness constants, see Section S4 of SM for the details. We fit the compiled thermal conductivity measurements with power-law functions of the corresponding $\bar{c}_i^2/\bar{c}_j^2$, i.e., $\frac{\Lambda_i}{\Lambda_j}=A\left(\frac{\bar{c}_i^2}{\bar{c}_j^2}\right)^n$, where the prefactor A and exponent n are fitting parameters. We summarize the fitted values of A and n in Table 2. Interestingly, we find that while the heat transport anisotropy both in and across basal planes is proportional to $\bar{c}_i^2/\bar{c}_j^2$, a prefactor of 3.7 instead of unity is observed in the cross-plane direction, see Figure 2 and Table 2.

Table 1. Measured anisotropic thermal conductivity and averages of speeds of sound from first-principles calculations in 2H-, 1T'- and Td-$MoTe_2$

Properties	2H-$MoTe_2$ (300 K)		1T'-$MoTe_2$ (300 K)			Td-$MoTe_2$ (80 K)		
	a axis	*c* axis	*a* axis	*b* axis	*c* axis	*a* axis	*b* axis	*c* axis
Λ_i (W m^{-1} K^{-1})	19	2.5	6.8	7.2	0.95	6.2	6.8	1.1
Λ_a/Λ_b	-		0.94			0.91		
Λ_a/Λ_c	7.6		7.2			5.6		
$\overline{c}_i$ (m s^{-1})	2702	2592	2786	2674	1909	2762	2741	1934
$\bar{c}_a^2/\bar{c}_b^2$	-		1.09			1.02		
$\bar{c}_a^2/\bar{c}_c^2$	1.08		2.13			2.04		

Table 2. Prefactors (A) and exponents (n) for power law fits to measurements (Figure 2) and calculations (Figure 3) of anisotropy of thermal conductivity (Λ_i/Λ_j), effective heat capacity ($C_{i,\mathrm{eff}}/C_{j,\mathrm{eff}}$), average group velocity ($\bar{v}_i^2/\bar{v}_j^2$), and average relaxation time ($\bar{\tau}_i/\bar{\tau}_j$).

Anisotropy ratios	Λ_i/Λ_j measurements		$C_{i,\mathrm{eff}}/C_{j,\mathrm{eff}}$ calculations		$\bar{v}_i^2/\bar{v}_j^2$ calculations		$\bar{\tau}_i/\bar{\tau}_j$ calculations	
Fitting parameters	A	n	A	n	A	n	A	n
In-plane	1.0	1.2	2.2	0.16	0.78	0.68	0.77	0.50

(i =a; j=b)								
Cross-plane (i =a or b; j=c)	3.7	1.1	8.2	0.12	1.1	0.46	0.37	0.45

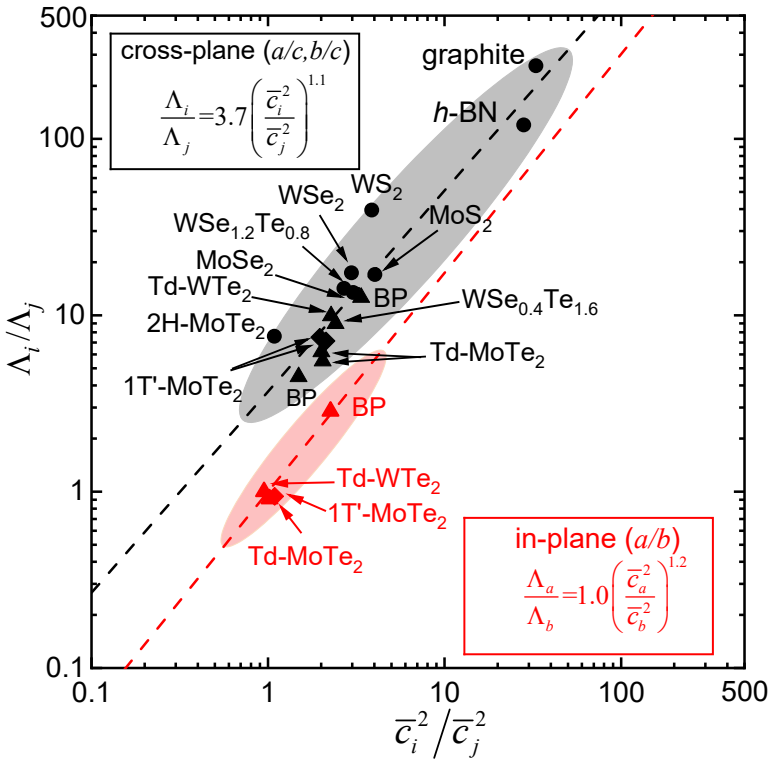

Figure 2. Anisotropy in thermal conductivity measurements Λ_i/Λ_j of a wide range of vdW materials [4,5,16,29-31,39] at 300 K (except for 80 K for Td-$MoTe_2$), as a function of anisotropy in the speeds of sound $\bar{c}_i^2/\bar{c}_j^2$. The red symbols represent in-plane anisotropy while the black symbols represent cross-plane anisotropy (i = a or b and j = c). Speeds of sound of h-BN, MoS_2, BP, and three phase $MoTe_2$ are from first-principles calculations in this work. Speeds of sound of other vdW materials are from prior experiments [40,41] and first-principles calculations [28,42-44]. The dashed lines are power law fits (equations in figure).

The apparent dependence of the thermal conductivity anisotropy on the speed of sound anisotropy is hard to justify from the perspective of phonon transport. First, in the calculation of $\bar{c}_i^2$ ($\bar{c}_i^2=\frac{1}{3}\sum c_{i,\alpha}^2$), it is implicitly assumed that heat is carried only by low-energy phonons and relaxation times in three acoustic branches (LA, TA, and ZA) are the same. The

assumptions contradict the fact that phonons of different frequencies [45,46], as well as phonons in different acoustic branches [14,47], play quite different roles in heat transport in different directions. Thus, $\bar{c}_i^2$, which is calculated only from the speeds of sound, do not fully capture the physics of the heat transport anisotropy.

To identify the origins of the heat transport anisotropy both in and across the basal planes, we propose a simple framework to assess the roles of anisotropies in phonon heat capacity, group velocity, and relaxation times to the heat transport anisotropy. In this framework, we approximate the thermal conductivity in direction i, Λ_i, as

$$\Lambda_i = C_{i,\text{eff}} \bar{v}_i^2 \bar{\tau}_i \tag{2}$$

where $C_{i,\text{eff}}$, $\bar{v}_i$ and $\bar{\tau}_i$ are the effective heat capacity, average group velocity and average relaxation time, respectively, in direction i, calculated from the modal heat capacities (C_q), phonon velocities ($\boldsymbol{v}_q$), and relaxation times (τ_q) of phonon mode q, over all phonons in the first Brillouin zone (FBZ):

$$\bar{v}_i^2 = \frac{\sum v_q^2 C_q \cos^2\theta_{q,i} \tau_q}{\sum C_q \cos^2\theta_{q,i} \tau_q} \tag{3a}$$

$$\bar{\tau}_i = \frac{\sum \tau_q v_q^2 C_q \cos^2\theta_{q,i}}{\sum v_q^2 C_q \cos^2\theta_{q,i}} \tag{3b}$$

$$C_{i,\text{eff}} = \sum_0^{\omega_{i,\text{cut}}} C_q \cos^2\theta_{q,i} \tag{3c}$$

More weight is put on phonons that contribute more significantly to heat transport in direction i, i.e., have larger wavevector components along i. For $\bar{v}_i$ and $\bar{\tau}_i$, remaining components of mode-dependent thermal conductivity in direction i are used as the weights, see Eq. (3) for the equations for the parameters. For $C_{i,\text{eff}}$, we include only predominant heat-carrying phonons

with frequencies less than a cutoff frequency, $\omega_{i,\mathrm{cut}}$, which is determined by thermal conductivity accumulation with frequency reaching 95% of heat transport in direction *i*, see Section S5 in SM for more details including the determination of $\omega_{i,\mathrm{cut}}$ values. As $C_{i,\mathrm{eff}}$ is different from the total heat capacity, $C_{i,\mathrm{eff}}$ cannot be independently measured by differential scanning calorimetry. Note that although heat capacity is a scalar property, $C_{i,\mathrm{eff}}$ depends on the heat flow direction through the $\cos^2\theta_{q,i}$ term and the fact that heat is carried in different directions primarily by different phonons. Again, we determine $\boldsymbol{v}_q$, τ_q and C_q from first principles calculations, see Methods.

Our framework, while not rigorously derived, can capture the essential physics of anisotropic heat transport as governed by anisotropies in phonon heat capacity, group velocity, and relaxation times. First, for a special case of all phonons in an isotropic material having the same phonon velocity *v* (simple Debye approximation) and relaxation time τ, Eq. (2) correctly reduces to $\frac{1}{3}C_{red}v^2\tau$, where C_{red} equals 95% of the total lattice heat capacity, as expected from the kinetic theory of phonons. Moreover, calculations of Eq. (2) correctly approximate to the first principles calculations of the anisotropic thermal conductivity of selected vdW materials (*h*-BN, MoS_2, $MoTe_2$ and BP) along crystallographic directions of *a*, *b*, and *c*, with a root-mean-square deviation of only 23 %, see Figure S7 in the Section S5 of the SM. This agreement, despite the simplicity of our framework, suggests that the model successfully captures the essential physics of anisotropic heat transport.

In Figure 3, we show the anisotropy ratios of the derived $C_{i,\mathrm{eff}}$, $\bar{v}_i$, and $\bar{\tau}_i$ across (for directions *a* and *c* or directions *b* and *c*) and along (for directions *a* and *b*) the basal planes against the respective $\bar{c}_i^2/\bar{c}_j^2$ from the same first-principles calculations. We fit the anisotropy

ratios with power-law functions and compare the fitted values of the prefactor A and exponent n for the effective heat capacity, average phonon velocity, and average relaxation times in Table 2. Though the fitting is far from perfect, the crude trend is sufficient to isolate the contributions of heat capacity, phonon velocity, and relaxation times to the thermal conductivity anisotropy.

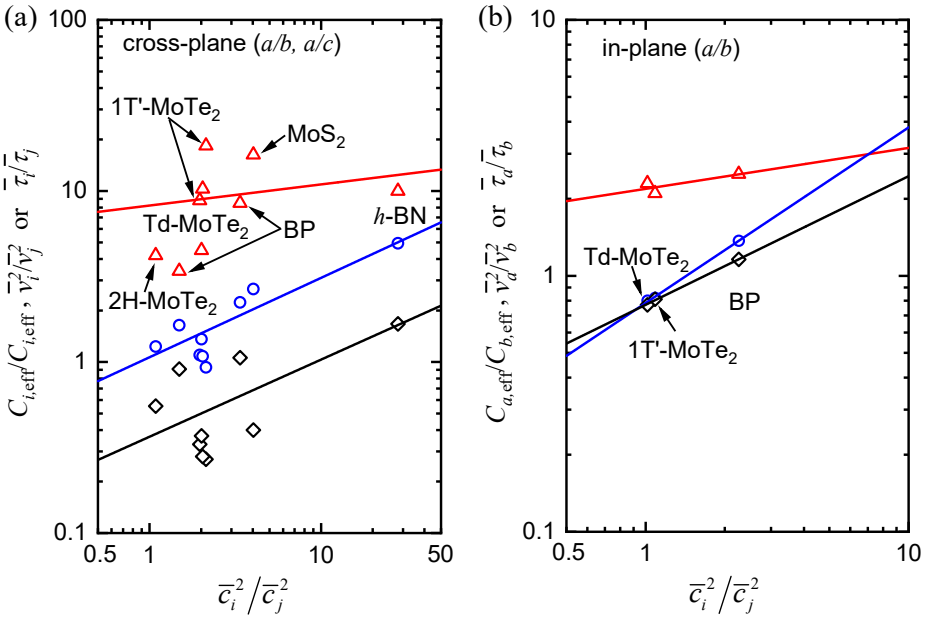

Figure 3. Anisotropy ratios of $C_{i,\mathrm{eff}}$, $\bar{v}_i$, and $\bar{\tau}_i$ **(a)** across (for directions a/c or b/c) and **(b)** along (for directions a/b) the basal planes. The values are calculated from our first-principles calculations using Eq. (3). Solid lines are fitted power laws with prefactors A and exponent n listed in Table 2.

We draw a few observations from the plots of $C_{i,\mathrm{eff}}$, $\bar{v}_i$, and $\bar{\tau}_i$ in Figure 3 and the values of A and n in Table 2. First, we find that while the anisotropy in effective heat capacity ($C_{i,\mathrm{eff}}$) is roughly independent of $\bar{c}_i^2/\bar{c}_j^2$ in both cross-plane and in-plane directions, the prefactor in the cross-plane direction is ~ 4 times larger than that in the in-plane direction, see Table 2. The factor of ~ 4 corresponds well with the prefactor of 3.7 that we observe from the

cross-plane anisotropy in the thermal conductivity measurements in Figure 2, suggesting that anisotropy in the thermal conductivity primarily originates from anisotropy in heat capacity.

To further understand the large anisotropy in the cross-plane direction, we closely examine the first principles calculations of 1T′-$MoTe_2$, which has similar speeds of sound in three crystallographic directions *a*, *b*, and *c*. We calculate and plot the accumulative heat capacity of 1T′-$MoTe_2$ along direction *i* (i.e., *a*, *b*, and *c*), $C_{i,\mathrm{acc}}(\omega) = \sum_0^{\omega} C_q \cos^2\theta_{q,i}$, as a function of frequency ω in Figure 4(a). We plot both the absolute values $C_{i.\mathrm{acc}}(\omega)$ and the normalized values $C_{i.\mathrm{acc}}(\omega)/C_{i.\mathrm{tot}}$, where $C_{i.\mathrm{tot}}$ is the summation of $C_q\cos^2\theta_{q,i}$ over all phonons in the materials as labelled in Figure 4(a). In the plot, we also include the cutoff frequency $\omega_{i,cut}$ in directions *a*, *b*, and *c*, and the corresponding $C_{i.\mathrm{eff}}/C_{i.\mathrm{tot}}$. We identify two factors contributing to the large cross-plane anisotropy in $C_{i,\mathrm{eff}}$. First, we find that $C_{i.\mathrm{tot}}$ is substantially smaller in the cross-plane direction, see Figure 4(a). Specifically, $C_{a,\mathrm{tot}}$ = 0.91 J cm^{-3} K, $C_{b,\mathrm{tot}}$ = 0.50 J cm^{-3} K, and $C_{c,\mathrm{tot}}$ = 0.14 J cm^{-3} K, respectively. $C_{i.\mathrm{tot}}$ is higher along the basal planes because there are more high-energy phonon modes propagating along basal planes in the anisotropic FBZ of vdW materials, as discussed and demonstrated previously in anisotropic Debye models for layered materials [20,48]. Second, we find that while ≈ 50 % of thermally excited phonons contribute to heat transport in both *a* and *b* directions, only 18 % contribute to heat transport in the *c* direction, see the ratios of $C_{i.\mathrm{eff}}/C_{i.\mathrm{tot}}$ in Figure 4(a). Contradictory to heat transport in the basal planes, heat is carried predominantly by low-frequency phonons across the basal planes [45] and high-frequency phonons that carry a large amount of heat are strongly scattered in the cross-plane direction, as suggested in prior first-principles calculations of BP [19] and MoS_2 [45]. The disparity in the frequency of the heat-carrying phonons along and across the basal planes

further leads to large heat capacity anisotropy.

The second observation we have from Figure 3 is that for both in-plane and cross-plane directions, $\bar{v}_i^2\bar{\tau}_i/\bar{v}_j^2\,\bar{\tau}_j$ is roughly proportional to $\bar{c}_i^2/\bar{c}_j^2$. Thus, the apparent linear dependence of the thermal conductivity anisotropy on $\bar{c}_i^2/\bar{c}_j^2$ originates from the anisotropy in both $\bar{v}_i^2$ and $\bar{\tau}_i$, not just $\bar{v}_i^2$ alone. For $\bar{v}_i^2$, we find that the exponent $n \approx 0.5$ and not unity, i.e., $\bar{v}_i^2$ scales with $\bar{c}_i$ instead of $\bar{c}_i^2$. One possible explanation to the deviation is that materials with high c_i usually have more phonons with higher energies that are not thermally excited compared to materials with low c_i, and thus the weaker dependence on $\bar{c}_i$. Interestingly, we find that $\bar{\tau}_i/\bar{\tau}_j$ have similar dependence on $\bar{c}_i^2/\bar{c}_j^2$ as $\bar{v}_i^2/\bar{v}_j^2$. This is consistent with the empirical relationship for Umklapp scattering of phonons, $\tau \propto v^2$ [49].

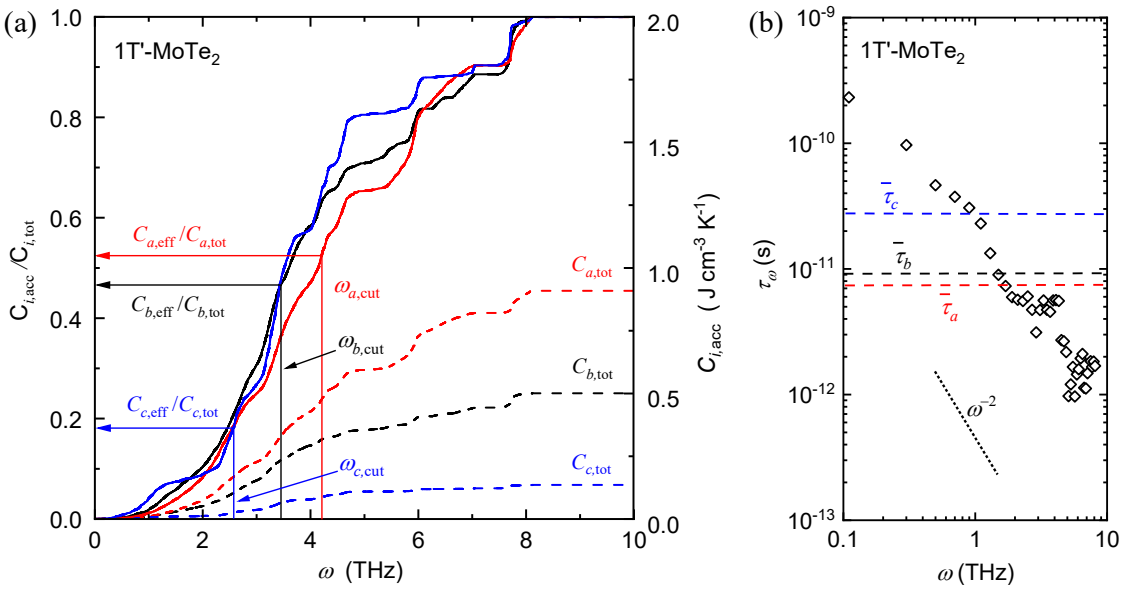

Figure 4: (a) Accumulative heat capacity ($C_{i,\mathrm{acc}}(\omega)$), in the in-plane directions *a* (red), *b* (black) and the cross-plane direction *c* (blue), in absolute (right axis) and normalized (left axis) values. The cutoff frequencies $\omega_{i,\mathrm{cut}}$ for three directions, and the corresponding $C_{i,\mathrm{eff}}(\omega)/C_{i,\mathrm{tot}}$, are labelled accordingly. **(b)** Frequency-dependent relaxation times τ_ω of 1T′-$MoTe_2$ from our first-

principles calculations. The dashed horizontal lines are average relaxation times $\bar{\tau}_i$ derived using Eq. (3b). The dotted line shows the $\tau_\omega \sim \omega^{-2}$ dependence.

Finally, we consider the effects of the anisotropy in relaxation times to heat transport anisotropy. We find that in the cross-plane direction, the prefactor A for the average relaxation time is only 0.37, see Table 2, substantially smaller than unity. $A < 1$ implies that the average relaxation time is *larger* in the cross-plane direction if the speeds of sound are isotropic. The larger relaxation times in the cross-plane direction are primarily due to the disparity in the frequency of the dominant heat-carrying phonons in the in-plane and cross-plane directions. To demonstrate this point, we determine the frequency-dependent relaxation times τ_ω from the arithmetic mean of modal relaxation times (τ_q) of all phonons with a frequency of $\omega \pm 0.1$ THz, and plot τ_ω as function of ω in Figure 4(b). We find that τ_ω scales with ω^{-2}, consistent with the ω-dependence of Umklapp processes for low-frequency phonons, derived by Klemens [50]. In the same figure, we also include the average relaxation times ($\bar{\tau}_i$) we derive using Eq. (3b). The average relaxation times in the cross-plane direction ($\bar{\tau}_c$) and in-plane directions ($\bar{\tau}_a$ and $\bar{\tau}_b$) correspond to τ_ω of 0.95 THz and 1.60 THz phonons, respectively, suggesting that heat is carried mainly by low-frequency phonons across the basal planes. Thus, the disparity in the frequency of the heat-carrying phonons along and across basal planes leads to two opposite effects – a large anisotropy in $C_{i,\mathrm{eff}}(\omega)$ that strengthens the heat transport anisotropy across the basal planes and a moderate anisotropy in $\bar{\tau}_i$ that reduces the heat transport anisotropy.

In summary, we investigated the origins of heat transport anisotropy in vdW layered materials through TDTR measurements and first-principles calculations of anisotropic thermal conductivity of three different phases of $MoTe_2$. We find that despite a weak anisotropy in the

speeds of sound, the thermal conductivity of all three phases of $MoTe_2$ is 5 – 8 times smaller in the cross-plane direction. Using a simple framework, we conclude that the heat transport anisotropy originates mainly from a large anisotropy in effective heat capacity. Further analysis suggests that both the highly anisotropic phonon dispersion of vdW materials and the disparity in the frequency of heat-carrying phonons contribute to the large anisotropy in effective heat capacity. Interestingly, the disparity in the frequency of heat-carrying phonons also leads to larger average relaxation times in the cross-plane direction, and thus reduces the cross-plane heat transport anisotropy. Our work provides new insight into the understanding of anisotropic heat transport in vdW layered materials.

Acknowledgment

This work was supported by the Singapore Ministry of Education Academic Research Fund Tier 2, under Award No. MOE2019-T2-2-135. L. L. acknowledges support for first principles calculations from the U.S. Department of Energy, Office of Science, Basic Energy Sciences, Materials Sciences and Engineering Division and computing resources from the National Energy Research Scientific Computing Center, which is supported by the Office of Science of the U.S. Department of Energy under Contract No. DE-AC02-05CH11231. T. P. acknowledges the support from the Research Foundation - Flanders (FWO-Vl)).

Methods

Sample characterization

Our 2H- and 1T′-$MoTe_2$ samples were purchased from HQ-Graphene. For easier handling, the 1T′-$MoTe_2$ sample is mounted on a silicon wafer with thermally conducive Ag

paint. We verified phases of our samples (i.e., the 2H and 1T′ phases at 300 K and the Td phase at 80 K) by Raman spectroscopy. The positions of observed peaks and the ratios of peak intensities for the three phases are consistent with those in the literature [51,52]. The splitting of the peak at 130 cm^{-2} into two close peaks indicates that a phase transition from 1T′-$MoTe_2$ to Td-$MoTe_2$ occured in our measurements [51-54].

We determined the crystallographic orientations of the 1T′-$MoTe_2$ and Td-$MoTe_2$ by polarized Raman spectroscopy [55,56]. The setup is under parallel polarized configuration and the incident light is horizontally polarized. We rotated the 1T′-$MoTe_2$ and Td-$MoTe_2$ samples in 15 degree increments and recorded the Raman signals within 100 cm^{-1} to 300 cm^{-1}. The crystallographic orientations were identified based on the integrated intensities of A_g mode at 164 cm^{-1} [55], see Section S1 of SM for more details.

TDTR measurements

We employed TDTR [57] and beam-offset TDTR [58] to determine the cross-plane and in-plane Λ of $MoTe_2$, respectively. In TDTR, a train of 787-nm beam from a mode-locked Ti:sapphire laser is split into a pump beam and a probe beam. The pump beam modulated at a frequency f is used to heat the sample, while the temperature oscillation at the sample surface is then recorded by monitoring the temperature-induced changes in the intensity of the reflected probe beam. Λ_c of samples is derived by comparing the measured signal to an analytical solution of a thermal diffusion model. In beam-offset TDTR, the out-of-phase signal (V_{out}) at a delay time of -100 ps is used to extract Λ_a and Λ_b. More details of TDTR and beam-offset TDTR can be found in literature [57,58] and Section S2 of the SM.

We carefully ensure that our TDTR and beam-offset TDTR measurements are not

affected by non-equilibrium phonons due to heating at high modulation frequencies [59] and small laser spot sizes [25]. We observed a strong frequency dependence in the derived Λ_c of the 2H-$MoTe_2$ sample, at 300 K and 100 K. We do not observe any obvious spot size dependence in all our measurements. These observations are consistent with the results in prior TDTR measurements for other vdW materials (e.g., MoS_2 [60], WSe_2 [4], and BP [5]). To obtain the intrinsic Λ_a, Λ_b, and Λ_c, we used a sufficiently low modulation frequency (f = 0.2 MHz) for all measurements, see Section S3 in SM for full discussion on frequency and spot size dependence of our measurements.

First-principles calculations

Theoretical calculations were performed with first-principle ab initio density functional theory (DFT) using Vienna Ab Initio Simulation Package (VASP) [61,62]. DFT calculations were performed within the projector augmented wave (PAW) method [63] with the generalized gradient approximation (GGA) according to Perdew, Burke, and Ernzerhof [64]. Twelve valence electrons for Mo ($4p^6$,$5s^1$,$4d^5$), and 6 for Te ($5s^2$, $5p^4$) were used in the PAW potentials. All the crystal structures were fully relaxed (both positions and volume) by employing a conjugate gradient scheme until the forces on every atom were minimized to be less than 0.005 eV/Å. A well-converged energy cutoff of 550 eV along with Gamma centered k point grids of 15×15×5, 7×15×3, and 15×7×3 were used for structure relaxation of 2H, 1T′, and Td phases, respectively. The inter-layer vdW interactions were treated by Grimme's DFT-D2 method [65]. Temperature dependence of the lattice parameters were not considered in our calculations, due to its negligible effect on the lattice thermal conductivity and the heat transport anisotropy, see Section S6 in the SM for more details.

Harmonic interatomic force constants (IFCs) of $MoTe_2$ allotropes are calculated within the finite difference method as implemented in the phonopy code [66,67]. Phonon calculations for 2H, 1T′, and Td phases were performed on 5×5 ×2 (300 atoms), 3×5×2 (360 atoms), and 5×3×2 (360 atoms) supercells using only the Gamma point. To obtain accurate phonon frequencies, a high energy cutoff of 600 eV and a strict energy convergence criterion of 10^{-8} eV were used. Anharmonic IFCs of $MoTe_2$ were calculated on the 5×5×2, 3×4×1, and 4×3×1 supercells for 2H, 1T′, and Td phases respectively. For the displaced supercell configurations, atomic interactions were truncated at 5.5 Å cut-off distance for all three phases. An energy cutoff of 500 eV, an energy convergence criterion of 10^{-7} eV, and Gamma point only Brillouin zone sampling were used.

The calculated harmonic and anharmonic IFCs were used to calculate phonon relaxation times (lowest order quantum perturbation theory) and the lattice thermal conductivity by solving phonon Boltzmann transport equations, as implemented in the ShengBTE package [68-70]. In our calculations, resistance from three-phonon scattering and isotopic disorder scattering [71] from natural isotope mass variations are included. For the lattice thermal conductivity and relaxation rates reported here, a Gaussian smearing width of 1.0 was used to approximate the energy conserving delta functions for each scattering process. Brillouin zone integrations were performed on 19×19×8, 12×24×8, and 24×12×8 sampling grids for 2H, 1T′, and Td phases, respectively.

References

[1] Debo Hu, Xiaoxia Yang, Chi Li, Ruina Liu, Ziheng Yao, Hai Hu, Stephanie N Gilbert Corder, Jianing Chen, Zhipei Sun, and Mengkun Liu, Nature communications **8** (1), 1 (2017).

[2] Weiliang Ma, Pablo Alonso-González, Shaojuan Li, Alexey Y Nikitin, Jian Yuan, Javier Martín-Sánchez, Javier Taboada-Gutiérrez, Iban Amenabar, Peining Li, and Saül Vélez, Nature **562** (7728), 557 (2018).
[3] Jingsi Qiao, Xianghua Kong, Zhi-Xin Hu, Feng Yang, and Wei Ji, Nature communications **5** (1), 1 (2014).
[4] Puqing Jiang, Xin Qian, Xiaokun Gu, and Ronggui Yang, Advanced Materials **29** (36), 1701068 (2017).
[5] Bo Sun, Xiaokun Gu, Qingsheng Zeng, Xi Huang, Yuexiang Yan, Zheng Liu, Ronggui Yang, and Yee Kan Koh, Advanced Materials **29** (3) (2017).
[6] Qingsheng Zeng, Bo Sun, Kezhao Du, Weiyun Zhao, Peng Yu, Chao Zhu, Juan Xia, Yu Chen, Xun Cao, and Qingyu Yan, 2D Materials **6** (4), 045009 (2019).
[7] Cristina V Manzano, Begoña Abad, Miguel Muñoz Rojo, Yee Rui Koh, Stephen L Hodson, Antonio M Lopez Martinez, Xianfan Xu, Ali Shakouri, Timothy D Sands, and Theodorian Borca-Tasciuc, Scientific reports **6** (1), 1 (2016).
[8] Shi En Kim, Fauzia Mujid, Akash Rai, Fredrik Eriksson, Joonki Suh, Preeti Poddar, Ariana Ray, Chibeom Park, Erik Fransson, and Yu Zhong, Nature **597** (7878), 660 (2021).
[9] Li-Dong Zhao, Shih-Han Lo, Yongsheng Zhang, Hui Sun, Gangjian Tan, Ctirad Uher, Christopher Wolverton, Vinayak P Dravid, and Mercouri G Kanatzidis, Nature **508** (7496), 373 (2014).
[10] Tianli Feng and Xiulin Ruan, Journal of Nanomaterials **2014** (2014).
[11] DA Broido, L Lindsay, and TL Reinecke, Physical Review B **88** (21), 214303 (2013).
[12] Yunshan Zhao, Gang Zhang, Mui Hoon Nai, Guangqian Ding, Dengfeng Li, Yi Liu, Kedar Hippalgaonkar, Chwee Teck Lim, Dongzhi Chi, and Baowen Li, Advanced Materials **30** (50), 1804928 (2018).
[13] Zhi Guo, Amit Verma, Xufei Wu, Fangyuan Sun, Austin Hickman, Takekazu Masui, Akito Kuramata, Masataka Higashiwaki, Debdeep Jena, and Tengfei Luo, Applied Physics Letters **106** (11), 111909 (2015).
[14] Ankit Jain and Alan JH McGaughey, Scientific reports **5** (1), 1 (2015).
[15] Sangwook Lee, Fan Yang, Joonki Suh, Sijie Yang, Yeonbae Lee, Guo Li, Hwan Sung Choe, Aslihan Suslu, Yabin Chen, and Changhyun Ko, Nature communications **6** (1), 1 (2015).
[16] Yabin Chen, Chaoyu Chen, Robert Kealhofer, Huili Liu, Zhiquan Yuan, Lili Jiang, Joonki Suh, Joonsuk Park, Changhyun Ko, and Hwan Sung Choe, Advanced Materials **30** (30), 1800754 (2018).
[17] Boyang Zhao, Md Shafkat Bin Hoque, Gwan Yeong Jung, Hongyan Mei, Shantanu Singh, Guodong Ren, Milena Milich, Qinai Zhao, Nan Wang, and Huandong Chen, Chemistry of Materials **34** (12), 5680 (2022).
[18] Saikat Mukhopadhyay, Lucas Lindsay, and David J Singh, Scientific reports **6** (1), 1 (2016).
[19] Jie Zhu, Haechan Park, Jun-Yang Chen, Xiaokun Gu, Hu Zhang, Sreejith Karthikeyan, Nathaniel Wendel, Stephen A Campbell, Matthew Dawber, and Xu Du, Advanced Electronic Materials **2** (5), 1600040 (2016).
[20] Hongkun Li, Weidong Zheng, and Yee Kan Koh, Physical Review Materials **2** (12), 123802 (2018).
[21] Xiaokun Gu and CY Zhao, Journal of Applied Physics **123** (18), 185104 (2018).
[22] Juan Jiang, ZK Liu, Y Sun, HF Yang, CR Rajamathi, YP Qi, LX Yang, C Chen, H Peng,

and CC Hwang, Nature communications **8** (1), 13973 (2017).
[23] Yee Kan Koh and David G. Cahill, Physical Review B **76** (7) (2007).
[24] Yongjie Hu, Lingping Zeng, Austin J Minnich, Mildred S Dresselhaus, and Gang Chen, Nature nanotechnology **10** (8), 701 (2015).
[25] Austin J Minnich, JA Johnson, AJ Schmidt, Keivan Esfarjani, MS Dresselhaus, Keith A Nelson, and Gang Chen, Physical review letters **107** (9), 095901 (2011).
[26] RB Wilson and David G Cahill, Nature communications **5**, 5075 (2014).
[27] Xue-Jun Yan, Yang-Yang Lv, Lei Li, Xiao Li, Shu-Hua Yao, Yan-Bin Chen, Xiao-Ping Liu, Hong Lu, Ming-Hui Lu, and Yan-Feng Chen, npj Quantum Materials **2** (1), 31 (2017).
[28] Daniel O Lindroth and Paul Erhart, Physical Review B **94** (11), 115205 (2016).
[29] Takeshi Nihira and Tadao Iwata, Japanese Journal of Applied Physics **14** (8), 1099 (1975).
[30] Catalin Chiritescu, David G Cahill, Ngoc Nguyen, David Johnson, Arun Bodapati, Pawel Keblinski, and Paul Zschack, Science **315** (5810), 351 (2007).
[31] Xin Qian, Puqing Jiang, Peng Yu, Xiaokun Gu, Zheng Liu, and Ronggui Yang, Applied Physics Letters **112** (24), 241901 (2018).
[32] Lucas Lindsay, DA Broido, and TL Reinecke, Physical review letters **111** (2), 025901 (2013).
[33] G Jeffrey Snyder and Eric S Toberer, Materials for sustainable energy: a collection of peer-reviewed research and review articles from Nature Publishing Group, 101 (2011).
[34] Makoto Tachibana, Taras Kolodiazhnyi, and Eiji Takayama-Muromachi, Applied Physics Letters **93** (9), 092902 (2008).
[35] David G Cahill, Alexander Melville, Darrell G Schlom, and Mark A Zurbuchen, Applied Physics Letters **96** (12), 121903 (2010).
[36] JL Cohn, GS Nolas, V Fessatidis, TH Metcalf, and GA Slack, Physical Review Letters **82** (4), 779 (1999).
[37] Toshiro Takabatake, Koichiro Suekuni, Tsuneyoshi Nakayama, and Eiji Kaneshita, Reviews of Modern Physics **86** (2), 669 (2014).
[38] Chen Li, Hao Ma, Tianyang Li, Jinghang Dai, Md Abu Jafar Rasel, Alessandro Mattoni, Ahmet Alatas, Malcolm G Thomas, Zachary W Rouse, and Avi Shragai, Nano Letters **21** (9), 3708 (2021).
[39] Chao Yuan, Jiahan Li, Lucas Lindsay, David Cherns, James W Pomeroy, Song Liu, James H Edgar, and Martin Kuball, Communications physics **2** (1), 43 (2019).
[40] Visnja Babacic, David Saleta Reig, Sebin Varghese, Thomas Vasileiadis, Emerson Coy, Klaas-Jan Tielrooij, and Bartlomiej Graczykowski, Advanced Materials **33** (23), 2008614 (2021).
[41] Alexey Bosak, Michael Krisch, Marcel Mohr, Janina Maultzsch, and Christian Thomsen, Physical Review B **75** (15), 153408 (2007).
[42] Li Li, Zhao-Yi Zeng, Ting Liang, Mei Tang, and Yan Cheng, Zeitschrift für Naturforschung A **72** (4), 295 (2017).
[43] B Rahman Rano, Ishtiaque M Syed, and SH Naqib, Results in Physics **19**, 103639 (2020).
[44] LL Li, C Bacaksiz, Mohammad Nakhaee, R Pentcheva, FM Peeters, and M Yagmurcukardes, Physical Review B **101** (13), 134102 (2020).
[45] Amey G Gokhale, Dhvaneel Visaria, and Ankit Jain, Physical Review B **104** (11), 115403 (2021).

[46] Puqing Jiang, Xin Qian, Ronggui Yang, and Lucas Lindsay, Physical review materials **2** (6), 064005 (2018).
[47] Haifeng Wang, Yan Gao, and Gang Liu, RSC advances **7** (14), 8098 (2017).
[48] Zhen Chen and Chris Dames, Applied Physics Letters **107** (19), 193104 (2015).
[49] DT Morelli, JP Heremans, and GA Slack, Physical Review B **66** (19), 195304 (2002).
[50] PG Klemens, Proceedings of the Royal Society of London. Series A. Mathematical and Physical Sciences **208** (1092), 108 (1951).
[51] Huaihong Guo, Teng Yang, Mahito Yamamoto, Lin Zhou, Ryo Ishikawa, Keiji Ueno, Kazuhito Tsukagoshi, Zhidong Zhang, Mildred S Dresselhaus, and Riichiro Saito, Physical Review B **91** (20), 205415 (2015).
[52] Xiaoli Ma, Pengjie Guo, Changjiang Yi, Qiaohe Yu, Anmin Zhang, Jianting Ji, Yong Tian, Feng Jin, Yiyan Wang, and Kai Liu, Physical Review B **94** (21), 214105 (2016).
[53] Jaydeep Joshi, Iris R Stone, Ryan Beams, Sergiy Krylyuk, Irina Kalish, Albert V Davydov, and Patrick M Vora, Applied physics letters **109** (3), 031903 (2016).
[54] Kenan Zhang, Changhua Bao, Qiangqiang Gu, Xiao Ren, Haoxiong Zhang, Ke Deng, Yang Wu, Yuan Li, Ji Feng, and Shuyun Zhou, Nature communications **7** (1), 1 (2016).
[55] Qingjun Song, Haifeng Wang, Xingchen Pan, Xiaolong Xu, Yilun Wang, Yanping Li, Fengqi Song, Xiangang Wan, Yu Ye, and Lun Dai, Scientific Reports **7** (1), 1758 (2017).
[56] Ryan Beams, Luiz Gustavo Cançado, Sergiy Krylyuk, Irina Kalish, Berç Kalanyan, Arunima K Singh, Kamal Choudhary, Alina Bruma, Patrick M Vora, and Francesca Tavazza, ACS nano **10** (10), 9626 (2016).
[57] David G Cahill, Review of scientific instruments **75** (12), 5119 (2004).
[58] J. P. Feser and D. G. Cahill, Rev Sci Instrum **83** (10), 104901 (2012).
[59] Yee Kan Koh and David G Cahill, Physical Review B **76** (7), 075207 (2007).
[60] Puqing Jiang, Xin Qian, and Ronggui Yang, Review of Scientific Instruments **88** (7), 074901 (2017).
[61] Georg Kresse and Jürgen Furthmüller, Computational materials science **6** (1), 15 (1996).
[62] Georg Kresse and Daniel Joubert, Physical review b **59** (3), 1758 (1999).
[63] Peter E Blöchl, Physical review B **50** (24), 17953 (1994).
[64] John P Perdew, Kieron Burke, and Matthias Ernzerhof, Physical review letters **77** (18), 3865 (1996).
[65] Stefan Grimme, Journal of computational chemistry **27** (15), 1787 (2006).
[66] Atsushi Togo, Fumiyasu Oba, and Isao Tanaka, Physical Review B **78** (13), 134106 (2008).
[67] Atsushi Togo and Isao Tanaka, Scripta Materialia **108**, 1 (2015).
[68] Wu Li, Jesús Carrete, Nebil A Katcho, and Natalio Mingo, Computer Physics Communications **185** (6), 1747 (2014).
[69] Wu Li, Natalio Mingo, Lucas Lindsay, David A Broido, Derek A Stewart, and Nebil A Katcho, Physical Review B **85** (19), 195436 (2012).
[70] Wu Li, Lucas Lindsay, David A Broido, Derek A Stewart, and Natalio Mingo, Physical Review B **86** (17), 174307 (2012).
[71] Shin-ichiro Tamura, Physical Review B **27** (2), 858 (1983).